Biosensors and Bioelectronics 127 (2019) 126–134

Contents lists available at ScienceDirect

Biosensors and Bioelectronics

journal homepage: www.elsevier.com/locate/bios

Monolayer rubrene functionalized graphene-based eletrochemiluminescence biosensor for serum cystatin C detection with immunorecognition-induced 3D DNA machine

Min Zhao[a], Lijuan Bai[b], Wei Cheng[c], Xiaolei Duan[a], Haiping Wu[a], Shijia Ding[a,*]

[a] Key Laboratory of Clinical Laboratory Diagnostics (Ministry of Education), College of Laboratory Medicine, Chongqing Medical University, Chongqing 400016, China
[b] Engineering Technology Research Center for Pharmacodynamic Evaluation of Chongqing, College of Pharmacy, Chongqing Medical University, Chongqing 400016, China
[c] The Center for Clinical Molecular Medical detection, The First Affiliated Hospital of Chongqing Medical University, Chongqing 400016, China

ARTICLE INFO

Keywords:
Graphene
Monolayer rubrene
Electrochemiluminescence
3D DNA machine
Cystatin C

ABSTRACT

Only surficial molecules of eletrochemiluminescent (ECL) nanomaterials are the most reactive species in the typical ECL reaction. Herein, monolayer rubrene was assembled on the surface of graphene sheet to obtain monolayer rubrene functionalized graphene composite (G/mRub) with strong ECL emission by maximizing the surficial rubrene molecules. Based on G/mRub as the strong ECL emitter, an ultrasensitive "on-off" biosensor was developed to detect cystatin C (Cys C) in human serum with the help of a novel immunorecognition-induced enzyme-free 3D DNA machine. Benefiting from the strong ECL emission of G/mRub and the efficient signal amplification of 3D DNA machine, the established biosensor achieved high sensitivity for Cys C detection with linear range from 1.0 fg mL^{-1} to 10 ng mL^{-1} and limit of detection down to 0.38 fg mL^{-1}. In addition, this enzyme-free biosensing method was adopted to successfully detect the concentration of Cys C in human serum. Therefore, the G/mRub based ECL biosensor might provide a potential tool for protein detection in clinical diagnosis and a new avenue to prepare high-performance luminescent nanomaterials.

1. Introduction

Polycyclic aromatic hydrocarbons-based organic semiconductors with high quantum yield, prominent charge carrier mobility and excellent optoelectronic property have been developed as electrochemiluminescent (ECL) emitters in the early 1964 (Hercules, 1964). However, restricted to their poor water solubility, they were seldom applied in bioanalysis. In order to obtain aqueous ECL system, Bard's group (Dick et al., 2014) proposed an oil-in-water emulsion system of rubrene (Rub, a classical organic semiconductor), which could achieve well ECL response in aqueous solution. Nevertheless, this Rub-based emulsion system maintains stability only for hours and is difficult to modification. In terms of this issue, Yuan's group (Liu et al., 2017) prepared water dispersible bulk Rub microrods by re-precipitation method to obtain a stable ECL system in aqueous solution. However, only surficial molecules of such bulk Rub microrods were excited in a typical ECL process, so that the ECL performance of Rub microrods was seriously limited by the relatively low specific surface area. Two-dimensional (2D) graphene sheets possess large specific surface area, rich surface chemistry and excellent physical properties (*e.g.,* conductivity, solubility), which are usually developed as preeminent nanocarriers (Cao et al., 2018; Yang et al., 2018a; Gu et al., 2018; Jayakumar et al., 2018). Especially, the large delocalization structure of graphene permits polyaromatic hydrocarbon molecules to be assembled on the surface for forming monolayer *via* π-π interaction (Alaboson et al., 2011; Gan et al., 2015). Herein, monolayer Rub functionalized graphene composite (G/mRub) is prepared to promote the ECL performance by maximizing the surficial Rub molecules.

DNA machines have attracted increasing research interest in biosensors and diagnostic applications due to their advantages of the predictability, specificity and versatility (Zhu et al., 2018a; Zhang et al., 2018; Ma et al., 2018; Zheng et al., 2018; Wang et al., 2014). In a typical DNA machine, spontaneous reaction is an essential to power the mechanical motions of DNA in the one-dimensional (1D), two-dimensional (2D), or three-dimensional (3D) tracks (Li et al., 2017a; Seeman, 2010). For example, Fan's group (Qu et al., 2017) employed exonuclease III mediated DNA digestion to power a stochastic 3D DNA machine. Li et al. (Li et al., 2018a, 2018b) engineered a nicking endonuclease to propel the movement of 3D DNA machine. However, the working of these 3D DNA machines relies on the fuel provided by

* Corresponding author.
E-mail address: dingshijia@cqmu.edu.cn (S. Ding).

https://doi.org/10.1016/j.bios.2018.12.009

Available online 15 December 2018

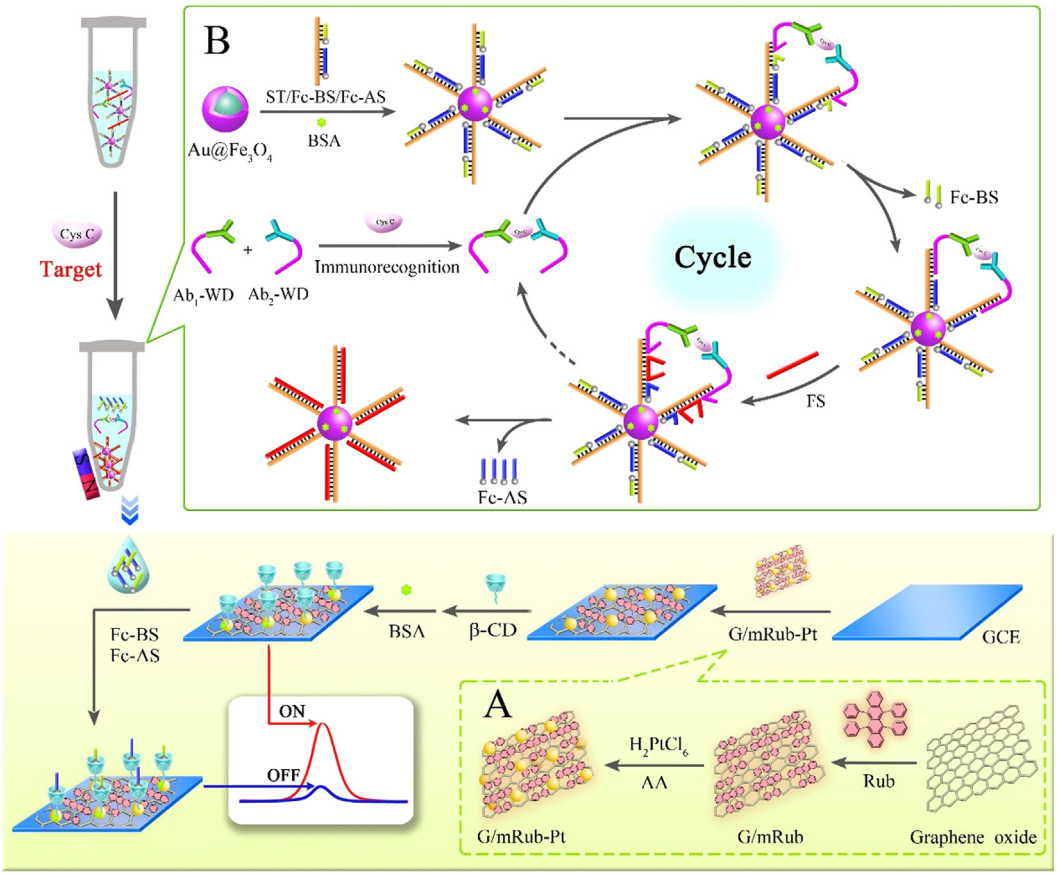

Scheme 1. The schematic illustration of the ultrasensitive "on-off" ECL biosensor for Cys C detection based on self-accelerated G/mRub-Pt composites and immunorecognition-induced 3D DNA machine. (A) The preparation process of G/mRub-Pt composites, (B) immunorecognition-induced 3D DNA machine amplification reaction.

enzymatic reaction, which increases the complexity of reaction system and the interference of enzyme inhibitor in clinical samples (Wu et al., 2018). Recently, the application of enzyme-free 3D DNA machine has required particular attention in clinical diagnoses (Li et al., 2017b; Jiang et al., 2017). Toehold-mediated strand displacement reaction is a typical enzyme-free spontaneous DNA reaction that can manage the movement of DNA molecules by meticulously designing the toeholds (Yang et al., 2018b; Khodakov et al., 2013). Thereby, enzyme-free 3D DNA machine is promising to be constructed using toehold-mediated strand displacement reaction to provide fuel.

Herein, an ultrasensitive "on-off" ECL biosensor is proposed on the basis of the novel G/mRub composites and immunorecognition-induced enzyme-free 3D DNA machine for the detection of cystatin C (Cys C) in serum samples. As shown in Scheme 1A, G/mRub composites are synthesized *via* one-step re-precipitation method. Then Pt nanoparticles (co-reaction accelerator) are *in situ* reduced on the surface of G/mRub to obtain self-accelerated ECL composites (G/mRub-Pt), which are coated onto the electrode surface to provide stable ECL signals as well as rich active sites for further modification. Subsequently, amino-modified β-cyclodextrin (β-CD) is assembled onto G/mRub-Pt modified electrode by Pt-N bond to obtain the high ECL signal state (signed as "signal-on"). Scheme 1B depicts the overall concept and the detection operation of the immunorecognition-induced 3D DNA machine. The 3D DNA machine is constructed on Au nanoparticles functionalized Fe_3O_4 ($Au@Fe_3O_4$) onto which are conjugated mass of three-stranded DNA complexes (ST/Fc-AS/Fc-BS). As a proof of principle, the target Cys C is specifically recognized by the capturing antibody-walking DNA conjugates (Ab_1-WD and Ab_2-WD) to form a sandwich immunocomplex (Ab_1-WD/Cys C/Ab_2-WD). And then the sandwich immunocomplex (Ab_1-WD/Cys C/Ab_2-WD) displaces the ferrocene-labeled blocker strand (Fc-BS) on 3D DNA machine *via* typical binding-induced DNA strand displacement, exposing the hidden toeholds. The exposed toeholds allow the fuel strand (FS) hybridize with ST, releasing the Ab_1-WD/Cys C/Ab_2-WD and ferrocene-labeled assistant strands (Fc-AS). The toehold-mediated strand displacement reaction provides the energy needed for Ab_1-WD/Cys C/Ab_2-WD complexes to autonomously and processively walk along the 3D DNA machine, achieving the massive release of Fc-AS and Fc-BS. The released Fc-AS and Fc-BS are further collected by magnetic separation and fabricated on the modified electrode *via* the guest-host recognition of Fc with β-CD. As Fc quenches the G/mRub-O_2 ECL system, the ECL signal decreases (signed as "signal-off") response to the increasing concentration of Cys C. With the efficient signal amplification of the 3D DNA machine, the biosensor exhibits high sensitivity for Cys C detection. Moreover, as the diverse advantages of free enzymes, high specificity and simple operation, immunorecognition-induced 3D DNA machine shows great potential for applications in bioanalysis.

2. Experimental methods

2.1. Materials and reagents

Rubrene (Rub), 3A-amino-3A-deoxy-(2AS, 3AS)-β-cyclodextrin (β-CD), chloroplatinic acid (H_2PtCl_6), gold chloride ($HAuCl_4$), ascorbic acid, N-hydroxysuccinimide (NHS), N-(3-(dimethylamino)propyl)-N′-ethylcarbodiimide hydrochloride (EDC) and bovine serum albumin (BSA) were brought from Sigma-Aldrich Chemical Co. (St. Louis, MO, U.S.A.). Graphene oxide was purchased from Xianfeng Nano Materials Tech Co. Ltd. (Nanjing, China). Sodium acetate trihydrate (NaAc), ferric chloride ($FeCl_3·6H_2O$), poly(ethylene glycol) (PEG), ethylene glycol, N,

N-dimethylformamide (DMF) were purchased from Kelong Chemical Inc. (Chengdu, China). Human cystatin C antigen (Cys C), monoclonal antibody 1 (Ab_1) and monoclonal antibody 2 (Ab_2) were purchased from CUSABIO Biotech. Co. Ltd. (Wuhan, China). The HPLC-purified DNA oligonucleotides were purchased from Shanghai Sangon Biological Engineering Technology & Services Co., Ltd. (Shanghai, China). The synthetic DNA sequences were listed in Table S1.

The phosphate buffer solution (PBS, pH 7.4) containing 0.5 M Na_2HPO_4, 0.5 M KH_2PO_4 and 0.1 M KCl was used as the electrolyte solution. All the solutions were prepared using deionized water (specific resistance of 18.2 MΩ cm). The colloidal Au nanoparticles (Au NPs) were prepared according to the reported literature with some modification (Liu and Lu, 2006).

2.2. Apparatus

The electrochemical and ECL measurements were executed with CHI660D electrochemistry workstation (Shanghai Chenhua Instruments, China) and MPI-E multifunctional analyzer (Xi'An Remax Electronic Science & Technology Co. Ltd., Xi'An, China), respectively. A conventional three-electrode system was consisted of a modified glass carbon electrode (working electrode), a Ag/AgCl electrode (reference electrode) and a platinum wire (counter electrode). The ECL spectrum was carried out by an electrochemical workstation combined with a Newton EMCCD spectroscopy detector (Andor Co., Tokyo, Japan). The morphologies of different nanomaterials were characterized by 7500 transmission electron microscope (TEM, Hitachi, Tokyo, Japan), S-4800 scanning electron microscopy (SEM, Hitachi, Tokyo, Japan) and Bruker Dimension Icon atomic force microscopy (AFM, Bruker, Germany). X-ray photoelectron spectroscopy (XPS) analysis was measured with VG Scientific ESCALAB 250 spectrometer operating by Al Ka X-ray (1486.6 eV) as the light source. The ultraviolet-visible (UV–vis) absorption and fluorescence spectra of different nanomaterials were performed with a UV-2450 UV–vis spectrophotometer (Shimadzu, Tokyo, Japan) and Cary Eclipse fluorescence spectrophotometer (Agilent Technologies, Palo Alto, CA) at room temperature in all experiments.

2.3. Preparation of G/mRub-Pt composites

The G/mRub-Pt composites were synthesized as shown in Scheme 1A. Firstly, 5 mg graphene oxide was dissolved in 20 mL deionized water by continuous ultrasonication, and then 0.5 mL orange rubrene DMF solution (2 mM) was added into above-mentioned graphene oxide aqueous solution and stirred at room temperature overnight to obtain G/mRub composites. Followed by centrifugation and dispersed with 10 mL deionized water, 400 μL H_2PtCl_6 aqueous solution (1.0 wt%) was added into the above solution and stirred at room temperature for 1 h. Under vigorous stirring, 1.0 mL of freshly prepared 100 mM ascorbic acid solution was quickly added in the above solution. With continuously stirring for 8 h at 65 °C, the solution changed from orange to gray. After centrifugation, the precipitates were collected and further washed with deionized water for three times to obtain G/mRub-Pt composites. The resultant product was dispersed in 1.0 mL deionized water and stored at 4 °C for further use.

2.4. Assembly of 3D DNA machines

Firstly, the mixture of the thiolated substrate DNA (ST, 2.5 μM), ferrocene-labeled blocker strand (Fc-BS, 3.0 μM), and ferrocene-labeled assistant strand (Fc-AS, 3.0 μM) in 20 mM Tris buffer (20 mM Tris-HCl and 2 mM $MgCl_2$, pH 7.4) was heated to 95 °C for 5 min and then naturally cooled down to room temperature to form the three-stranded DNA complexes (ST/Fc-BS/Fc-AS). Next, the obtained ST/Fc-BS/Fc-AS complexes were treated with 10 mM tris(2-carboxyethyl)phosphine hydrochloride (TCEP) for 1 h. Followed, Au NPs encapsulated Fe_3O_4 composites (Au@Fe_3O_4) were added to the above solution, which was synthesized as the description in the Supplementary materials. After keeping for 12 h, BSA (0.25%) was added and then reacted for 60 min to block the nonspecific adsorption sites (BSA/ST/Fc-BS/Fc-AS/Au@Fe_3O_4). Then magnetic separation was executed to remove the upper solution. The residue was washed with PBS for 3 times to obtain the resultant 3D DNA machines, which were dispersed in 1.0 mL PBS and stored at 4 °C when not in use.

2.5. Preparation of Ab_1-WD and Ab_2-WD

The walker DNA-labeled Ab_1 (Ab_1-WD) and walker DNA-labeled Ab_2 (Ab_2-WD) were prepared by the same steps. Firstly, 10 μL of 100 μM carboxyl groups-modified WD was added into 500 μL of PBS (pH 7.4) containing 40 mM EDC and 10 mM NHS and then stirred for 2 h at 4 °C. Next, 12 μL of 7.8 mg mL^{-1} capturing antibody 1 (Ab_1) was added into the above mixture and reacted for overnight at 4 °C. Last, Ab_1-WD was prepared, and so did Ab_2-WD.

2.6. Polyacrylamide gel electrophoresis (PAGE)

The samples were loaded into the notches of the freshly prepared native polyacrylamid gel (12%), and electrophoresis was performed at 110 V for 70 min in 1 × TBE buffer (89 mM Tris-boric acid, 2 mM EDTA, pH 8.3). After dying with gold view II, the gel was transferred to dark box for gel imaging.

2.7. Fabrication of ECL biosensor

The glassy carbon electrode (GCE, 3 mm in diameter) was pretreated according to the previously reported method (Zhao et al., 2015). Concretely, GCE was successively polished with 0.3 μm and 0.05 μm alumina slurries and then ultrasonicated in deionized water to obtain a mirror-like electrode. Next, 5 μL of prepared G/mRub-Pt composites was dropped onto GCE and dried at room temperature to form a uniform film. Subsequently, 10 μL of 10 mM amino-terminated β-CD was attached by incubating at room temperature for overnight. The modified electrode was then rinsed with deionized water to remove the uncombined β-CD and then incubated with 10 μL of 0.25% BSA for 60 min to eliminate nonspecific binding sites. Finally, the fabricated ECL biosensor was stored at 4 °C when not in use.

2.8. ECL measurement procedure

Initially, the immunorecognition-induced 3D DNA machine amplification reaction was implemented with the fabricated ECL biosensor as follows. 20 μL of prepared 3D DNA machine, 5 μL of 2 μM FS, 5 μL of Ab_1-WD, 5 μL of Ab_2-WD, 5 μL of various concentrations Cys C and 10 μL of 0.1 M PBS were added into EP tube and reacted for 120 min at 37 °C. Followed by magnetic separation to collect supernatant, 10 μL of supernatant was dropped onto the fabricated ECL biosensor and then incubated for 60 min at room temperature.

The ECL measurement was executed with the MPI-E ECL analyzer by scanning the potential from −1.0–0.8 V with a scan rate of 0.2 V/s in 2 mL of 0.1 M PBS (pH 7.4). The changes of ECL intensity (ΔI), defined as $\Delta I = I_0 - I$ (where I represented the ECL intensity with samples and I_0 represented the ECL intensity with blank), were positively related to Cys C concentrations.

3. Results and discussion

3.1. Characterization of G/mRub-Pt composites

The morphological changes in the synthetic process of G/mRub-Pt composites were monitored by scanning electron microscopy (SEM). Fig. 1A described the large lamellate and scrolled sheets with irregular size, representing the graphene oxide sheets (Li et al., 2018a). When the

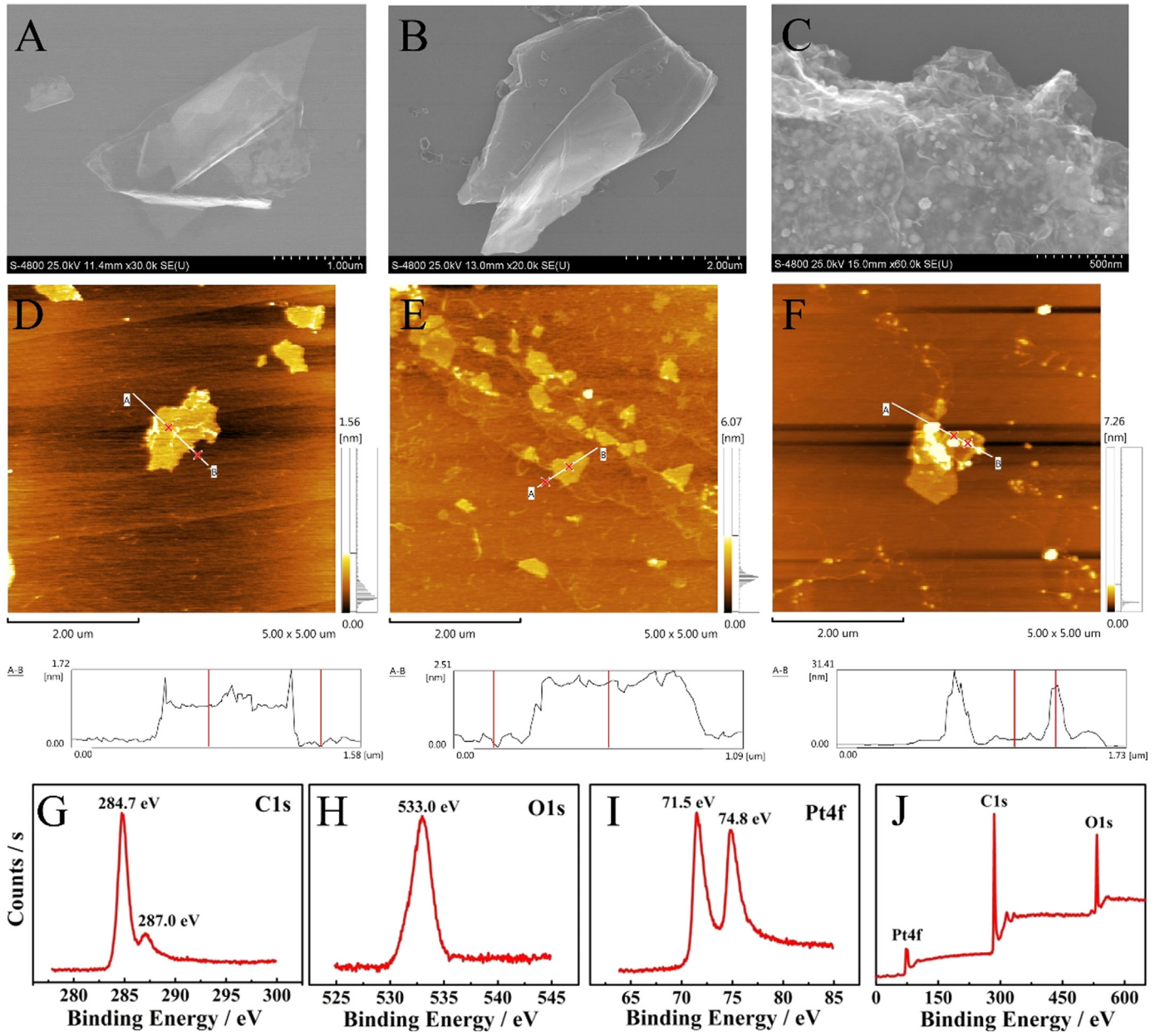

Fig. 1. SEM images of (A) graphene oxide, (B) G/mRub and (C) G/mRub-Pt. AFM images of (D) graphene oxide, (E) G/mRub and (F) G/mRub-Pt with their height profiles. XPS analysis for (G) C1s region, (H) O1s region, (I) Pt4f region and (J) full region of G/mRub-Pt.

Rub molecules were assembled into the graphene oxide surface, little evolution in morphology was observed as the monolayer Rub was too thin to be observed by SEM (Fig. 1B). After decorating with Pt nanoparticles, as shown in Fig. 1C, numerous Pt nanoparticles were evenly distributed on the surface of G/mRub composites. The sheets and nanoparticles remained separated with each other without any aggregation, implying the well dispersibility of the G/mRub-Pt composites in solution.

To confirm the Rub monolayer on graphene surface, the thickness in the stepwise assembly process of G/mRub-Pt composites was characterized using the atomic force microscopy (AFM). Fig. 1D showed the typical AFM image of graphene oxide sheets. It was found that the substrate mica was covered with the average thickness about 0.9 nm of nanosheets. After the Rub molecules assembling into the surface of graphene oxide sheets, the thickness of the G/mRub composites increased to ~2.0 nm (Fig. 1E), verifying that the Rub molecules successfully assembled on the graphene sheet and a monolayer of Rub molecules (~0.55 nm) was obtained (Fumagalli et al., 2011; Pivetta et al., 2008; Zeng et al., 2008). When the Pt nanoparticles were *in situ* reduced onto the G/mRub composites, the mean thickness of the G/mRub-Pt composites increased to 25 nm (Fig. 1F), which was coincident with the SEM results.

Moreover, X-ray photoelectron spectroscopy (XPS) characterization was employed to investigate the elemental composition of G/mRub-Pt composites. Fig. 1G-J presented the characteristic peaks of C1s, O1s and Pt4f core level regions of G/mRub-Pt composites. The peaks at 284.7 eV and 533.0 eV were assigned to C1s and O1s, respectively, which manifested the presence of graphene and Rub. As expected, the XPS signature of Pt4f doublet (71.5 eV and 74.8 eV) indicated the presence of the metallic Pt°. These results proved the successful synthesis of the G/mRub-Pt composites.

In addition, the typical UV–vis absorption spectra were also used to characterize the G/mRub-Pt composite in Fig. 2. As exhibited in Fig. 2A, a characteristic UV–vis absorption peak centered at 230 nm

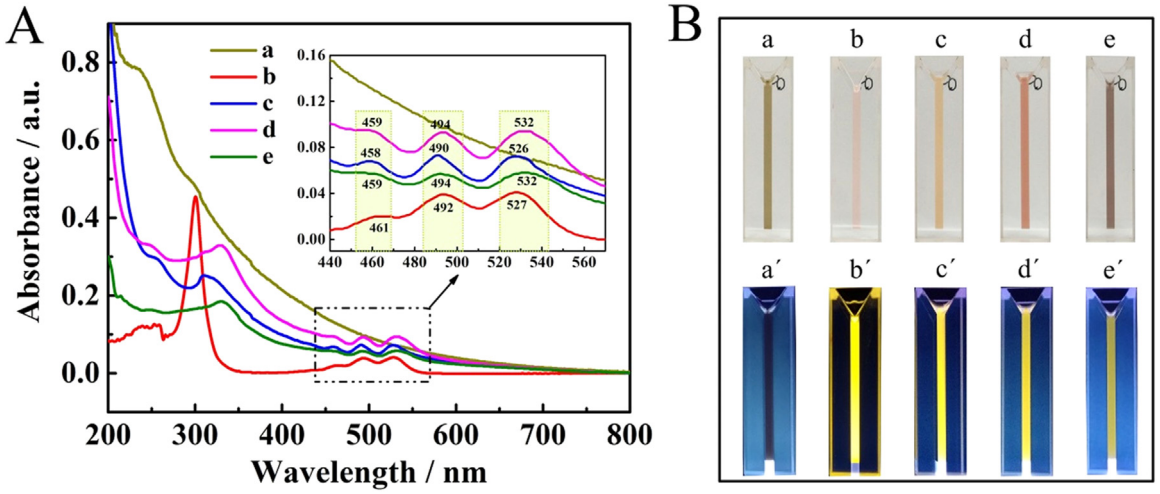

Fig. 2. (A) Typical UV–vis absorption spectra and (B) the photos of (a) graphene oxide, (b) Rub in DMF, (c) Rub NPs, (d) G/mRub and (e) G/mRub-Pt. The B was under the natural light (up) and UV light of 365 nm (down), respectively.

was observed in graphene oxide aqueous solution (curve a), which was assigned to π-plasmon of graphene oxide (Repp et al., 2018). The UV–vis absorption spectrum of Rub in DMF showed typical characteristic peaks at 300 nm and a broad band at 430–550 nm due to π-π^* transition (curve b) (Vinyard et al., 2008). However, when the Rub was prepared to Rub nanoparticles (Rub NPs) without surfactants in aqueous solution, the characteristic absorption peaks of Rub NPs emerged a slight bathochromic shift from 300 nm to 310 nm due to π-π interaction and a slight hypsochromic shift from 461, 492, 527 nm to 458, 490, 526 nm due to the increase of solvent polarity (curve c). Compared with the absorption spectra of graphene oxide and Rub NPs, the absorption spectrum of G/mRub showed more bathochromic shift to 245 nm, 330 nm, 459 nm, 494 nm and 532 nm, respectively (curve d). It was mainly due to the strong conjugation effect between graphene oxide and Rub molecules from G/mRub. After Pt nanoparticles were *in situ* reduced by ascorbic acid onto the surface of G/mRub, the characteristic absorption peak at 245 nm from graphene oxide gradually disappeared and little change was observed for the other characteristic absorption peaks (curve e). These results exhibited that the ascorbic acid not only reduced the H_2PtCl_6 into the Pt nanoparticles, but also reduced the graphene oxide into reduced graphene oxide.

3.2. Characterization of Au@Fe_3O_4 composites

The morphologies and sizes of Au@Fe_3O_4 were characterized by transmission electron microscope (TEM) and showed in Fig. S1. It revealed that the prepared Fe_3O_4 exhibited regular spherical particles with size distribution averaging about 200 nm (Fig. S1A). After functionalizing with Au nanoparticles, it could be seen that the Au nanoparticles with the size about 10 nm were unevenly distributed in the surface of Fe_3O_4 (Fig. S1B).

3.3. Characterization of the 3D DNA machine

The assembly of the 3D DNA machine has been verified by native polyacrylamide gel electrophoresis (PAGE) and zeta potential. As shown in Fig. S2A, the three-stranded DNA complexes (ST/Fc-BS/Fc-AS) in lane 1 exhibited a distinct single band. Lane 2 showed the PAGE result for the 3D DNA machine by assembling the ST/Fc-BS/Fc-AS onto Au@Fe_3O_4, exhibiting an unapparent band. This was an attribute that ST/Fc-BS/Fc-AS was assembled onto Au@Fe_3O_4 for the 3D DNA machine formation, leading to the great decrease of free ST/Fc-BS/Fc-AS. Moreover, zeta potential is well-known as an efficient tool for the monitoring and analysis of modifications on the surface of nanoparticles to obtain the nanoparticles surface charge. Since DNA is negatively charged, the conjugation of Au@Fe_3O_4 with DNA should give rise to negative charged conjugates which would shift the zeta potential to more negative values. As displayed in Fig. S2B, a shift of up to 11.3 mV in the zeta potential was observed with the Au@Fe_3O_4 after assembling ST/Fc-BS/FC-AS. These results suggested that Au@Fe_3O_4 was being assembled with negative charged ST/Fc-BS/Fc-AS to form 3D DNA machine.

3.4. Conductivity, hydrophilicity and optical properties of G/mRub

In order to explore the superiority of G/mRub, contrast experiments were carried out to compare the conductivity and hydrophilicity of G/mRub with Rub NPs under the same conditions. Firstly, electrochemical impedance spectroscopy (EIS) was performed in 5 mM $[Fe(CN)_6]^{4-/3-}$ containing 0.1 M KCl. As exhibited in Fig. 3A, the semicircle (curve b, Ret ≈ 396 Ω) of G/mRub was evidently lower than the semicircle (curve a, Ret ≈ 746 Ω) of Rub NPs, indicating that the conductivity of G/mRub was better than that of Rub NPs. Additionally, water contact angle measurement was performed on Rub NPs and G/mRub, respectively. Pictures of water droplets on the surface and the measured contact angles were shown in Fig. 3B. It displayed a contact angle of Rub NPs with 89.7° (a). Notably, the G/mRub manifested a contact angle of 47.0° (b), which was much less than that of Rub NPs. These confirmed that the G/mRub indeed possessed good hydrophilicity.

Optical properties of the G/mRub were characterized by phosphorescence (PL) and ECL spectra. As displayed in Fig. 3C, the PL maximum excitation wavelengths of G/mRub were at 469 nm, 498 nm, 531 nm (blue line), and the maximum emission wavelength was at 564 nm (red line), respectively. Additionally, the ECL emission spectrum of the G/mRub with the maximum emission wavelength was at 600 nm (Fig. 3D).

3.5. Electrochemical characterization of the ECL biosensor

In order to confirm the successful stepwise assembly of the ECL biosensor, the cyclic voltammograms (CVs) was applied in 0.1 M PBS (pH 7.4) containing 5 mM $[Fe(CN)_6]^{3-/4-}$. As exhibited in Fig. 4A, a pair of well-defined redox peaks of $[Fe(CN)_6]^{3-/4-}$ was obtained from the bare GCE (curve a). As expected, when the G/mRub-Pt composites were modified onto the surface of GCE, the current significantly increased (curve b), which was attributed to the excellent electric conduction of Pt nanoparticles and G/mRub from G/mRub-Pt composites. However, the redox peak current decreased after the assembly of non-conductive

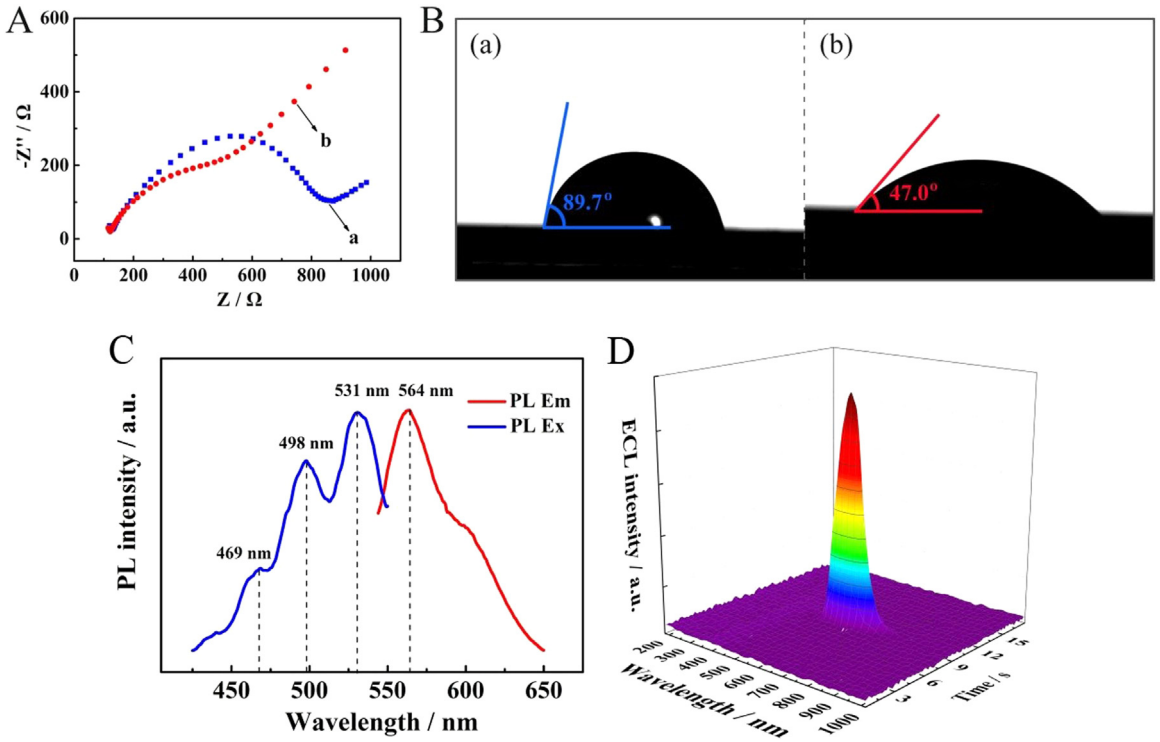

Fig. 3. (A) EIS profiles and (B) contact angle images of (a) Rub NPs and (b) G/mRub. (C) The PL spectra of G/mRub and (D) the ECL emission spectrum of G/mRub. The ECL emission spectrum was obtained by scanning the potential from − 1.0 to 0.8 V with a scan rate of 0.2 V/s in 2 mL of 0.1 M PBS (pH 7.4).

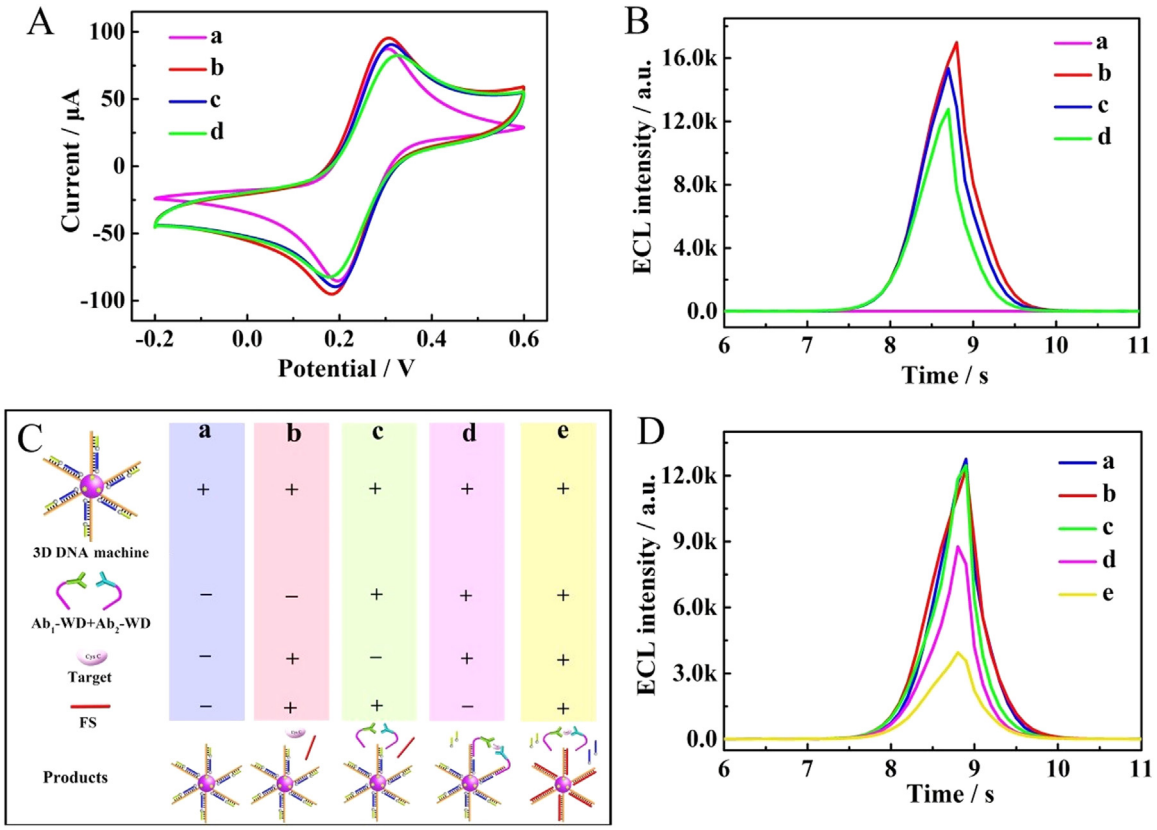

Fig. 4. (A) CVs performed in 0.1 M PBS (pH 7.4) containing 5 mM $[Fe(CN)_6]^{3-/4-}$ with the scan range of −0.2–0.6 V. (B) ECL-time profiles performed in 0.1 M PBS (pH 7.4) with the scan range of − 1.0–0.8 V and the photomultiplier tube of 800 V. (a) bare GCE, (b) G/mRub-Pt/GCE, (c) β-CD/G/mRub-Pt/GCE, (d) BSA/β-CD/G/mRub-Pt/GCE. (C) Schematic diagram of control experiments and (D) corresponding ECL responses of the modified electrodes (BSA/β-CD/G/mRub-Pt/GCE) incubated with the products of control experiments: (a) only 3D DNA machine, (b) 3D DNA machine + target + FS, (c) 3D DNA machine + Ab_1-WD + Ab_2-WD + FS, (d) 3D DNA machine + Ab_1-WD + Ab_2-WD + target, (e) 3D DNA machine + Ab_1-WD + Ab_2-WD + target + FS. The concentration of target Cys C was 1.0 ng mL^{-1}.

β-CD (curve c). Next, after blocking with the BSA, the redox peak current continuously decreased due to the biomacromolecule hindering the electron transfer (Zhu et al., 2018b) (curve d). These results indicated that the proposed biosensing platform was fabricated as designed.

Moreover, ECL measurement was also carried out to further confirm the interfacial processes at electrode surfaces. As shown in Fig. 4B, almost no ECL signal was seen on the bare GCE owing to the lack of emitters. When the G/mRub-Pt composites were immobilized onto the surface of GCE, a strong ECL signal was obtained (curve b). Upon the addition of β-CD and BSA, successive decreases of ECL signal were observed (curve c and d), which was attributable to the non-conductivity of β-CD and BSA. These results further demonstrated that the ECL sensing platform was successfully constructed as expected.

3.6. Feasibility analysis of the biosensor for Cys C detection

To estimate the feasibility of the developed biosensor for Cys C detection based on the immunorecognition-induced 3D DNA machine, a series of control experiments was performed by incubating the modified electrodes (BSA/β-CD/G/mRub-Pt/GCE) with different products. Here, the immunorecognition-induced 3D DNA machine was studied by selecting Ab_1-WD and Ab_2-WD, target, FS as the control conditions (Fig. 4C), and the corresponding ECL responses were shown in Fig. 4D. When there was only 3D DNA machine (column a, Fig. 4C), the ECL signal was 12,760 a.u. (curve a, Fig. 4D). When the target and FS were added into the 3D DNA machine (column b, Fig. 4C), the ECL signal about 12,305 a.u. (curve b, Fig. 4D) was as strong as curve a. Similarly, when the Ab_1-WD, Ab_2-WD and FS were added into the 3D DNA machine (column c, Fig. 4C), a strong ECL signal about 12,462 a.u. was obtained (curve c, Fig. 4D). These results were attributed that the sandwich immunoreaction was not formed to displace the Fc-BS and Fc-AS. However, when the Ab_1-WD, Ab_2-WD and target were added into the 3D DNA machine (column d, Fig. 4C), the ECL signal markedly decreased to 8772 a.u. (curve d, Fig. 4D). This was mainly because the Ab_1-WD/target/Ab_2-WD complexes were formed by sandwich immunoreaction, resulting in the release of Fc-BS from 3D DNA machine for further quenching the ECL signal of G/mRub-O_2 system. Interestingly, when the Ab_1-WD, Ab_2-WD, target and FS were mixed with 3D DNA machine (column e, Fig. 4C), the ECL signal sequentially reduced to 3947 a.u. (curve e, Fig. 4D). It was attributed that numerous Fc-BS and Fc-AS were released by proximity binding-induced displacement by Ab_1-WD/target/Ab_2-WD complexes and toehold-mediated strand displacement by FS to efficiently quench the ECL signal. These results indicated that immunorecognition-induced 3D DNA machine amplification strategy could significantly amplify target-relevant DNA output for the detection of target Cys C at low levels.

3.7. The possible enhancing luminous mechanisms of G/mRub-Pt and the quenching luminous mechanisms by Fc

The possible enhancing luminous mechanisms of G/mRub-Pt were described according to the reported literature (Liu et al., 2017) as follows.

$$G/mRub - e^- \rightarrow G/mRub^{\bullet +} \quad (1)$$

$$O_2 + e^- \xrightarrow[Pt]{} O_2^{\bullet -} \quad (2)$$

$$O_2 + 2H_2O + e^- \xrightarrow[Pt]{} H_2O_2 + 2OH^- \quad (3)$$

$$O_2^{\bullet -} + H_2O_2 \rightarrow O_2 + OH^- + OH^{\bullet} \quad (4)$$

$$G/mRub^{\bullet +} + O_2^{\bullet -} \rightarrow G/mRub^* + O_2 \quad (5)$$

$$G/mRub^{\bullet +} + OH^{\bullet} \rightarrow G/mRub^* + OH^- \quad (6)$$

$$G/mRub^* \rightarrow G/mRub + h\nu \quad (7)$$

First, the G/mRub lost an electron to form $G/mRub^{\bullet +}$ radical cation (Eq. (1)) under the positive potential scan of −1.0–0.8 V. Next, under the negative potential scan, the dissolved O_2 in the testing buffer was reduced to generate massive reactive oxygen species ($O_2^{\bullet -}$ and $OH^{\bullet}$) with the help of the co-reaction accelerator of Pt nanoparticles (Eqs. 2–4). The obtained $O_2^{\bullet -}$ and $OH^{\bullet}$ reacted with $G/mRub^{\bullet +}$ to generate the excited state $G/mRub^*$ (Eq. (5) and Eq. (6)). Finally, the enhanced ECL emission was obtained with $G/mRub^*$ returning back to the ground state (Eq. (7)).

In order to validate the ECL quenching mechanism, the ECL-potential and synchronous CV curves of the biosensors were investigated in the presence and absence of Fc. Specifically, the prepared biosensor (BSA/β-CD/G/mRub-Pt/GCE) was measured before (blue line) and after (red line) the incubation with 10 μL of 1.0 mM Fc. As shown in Fig. S3, when the biosensor was incubation with Fc, a reduction wave at −0.80 V attributed to the reduction of O_2 (Deng et al., 2011) was significantly increased, and a pair of redox peaks at 0.44 V and 0.42 V attributed to the redox of Fc was observed (red line). These results indicated that the addition of Fc increased the electrochemical reduction of O_2 at the surface of modified electrode (Eq. (2) and Eq. (3)), which could be ascribed to the consumption of $OH^{\bullet}$ by $Fc(Fe^{II})$ (Watts and Dilly, 1996; Lagos and Reyes, 1988). The consumption of $OH^{\bullet}$ would result in the decrease of ECL intensity, which was confirmed by the ECL responses from 12,460 a.u. down to 656 a.u. The possible mechanisms were as follows.

$$4Fc(Fe^{II}) + OH^{\bullet} \rightarrow 4Fc(Fe^{III}) + OH^- \quad (8)$$

$$Fc(Fe^{III}) + e^- \rightarrow Fc(Fe^{II}) \quad (9)$$

Concretely, $Fc(Fe^{II})$ reacted with the $OH^{\bullet}$ to form $Fc(Fe^{III})$ (Eq. (8)), resulting in the consumption of $OH^{\bullet}$ for ECL decrease. Then, the $Fc(Fe^{III})$ was reduced to $Fc(Fe^{II})$ under cathodic potential scanning (Eq. (9)) to regenerate the $Fc(Fe^{II})$ for competing $OH^{\bullet}$ with $G/mRub^{\bullet +}$.

3.8. Analytical performance of the proposed biosensor

Under the optimal condition (see Fig. S4 of Supplementary materials), the analytical performance of the biosensor was investigated. As the results displayed in Fig. 5A and B, the ECL signal decreased accordingly upon the increase of Cys C concentrations in the range from 1×10^{-3} to 1×10^4 pg mL^{-1}. And the calibration plot exhibited a favorable linear relationship between the changes of ECL intensities ($\triangle I_{ECL}$) and the logarithm value of Cys C concentrations, with a correlation coefficient of 0.9984. The regression equation was $\triangle I = 1288.8 \lg c + 4771.8$, and the limit of detection was calculated as 0.38 fg mL^{-1} (see Fig. S5 of Supplementary materials) according to the previously reported work (Long and Winefordner, 1983). Importantly, this developed biosensor for Cys C detection was more sensitive than those previously reported methods (Table S2), which was attributable to the high ECL performance of G/mRub and efficient signal amplification of enzyme-free 3D DNA machine.

To explore the selectivity of the biosensor, prostate-specific antigen (PSA), carcino-embryonic antigen (CEA), thrombin (TB), laminin (LN), and mucin 1 (MUC1) were selected as interfering substances. According to Fig. 5C, the biosensors were incubated with the interfering substances (PSA, CEA, TB, LN, MUC1) which were higher concentration (50-fold, 0.5 ng mL^{-1}) than target Cys C (10 pg mL^{-1}) showed no obvious effect on the ECL intensity. When the biosensor was incubated with the mixture containing PSA (0.5 ng mL^{-1}), CEA (0.5 ng mL^{-1}), TB (0.5 ng mL^{-1}), LN (0.5 ng mL^{-1}), MUC1 (0.5 ng mL^{-1}), and Cys C (10 pg mL^{-1}), there was no obvious difference compared with the ECL intensity of the pure 10 pg mL^{-1} Cys C. Those results manifested the superior selectivity of this biosensor.

Stability, another important performance of the biosensor, was estimated under consecutive cyclic potential scans when the biosensors were incubated with 10 fg mL^{-1} and 10 pg mL^{-1} of Cys C, respectively.

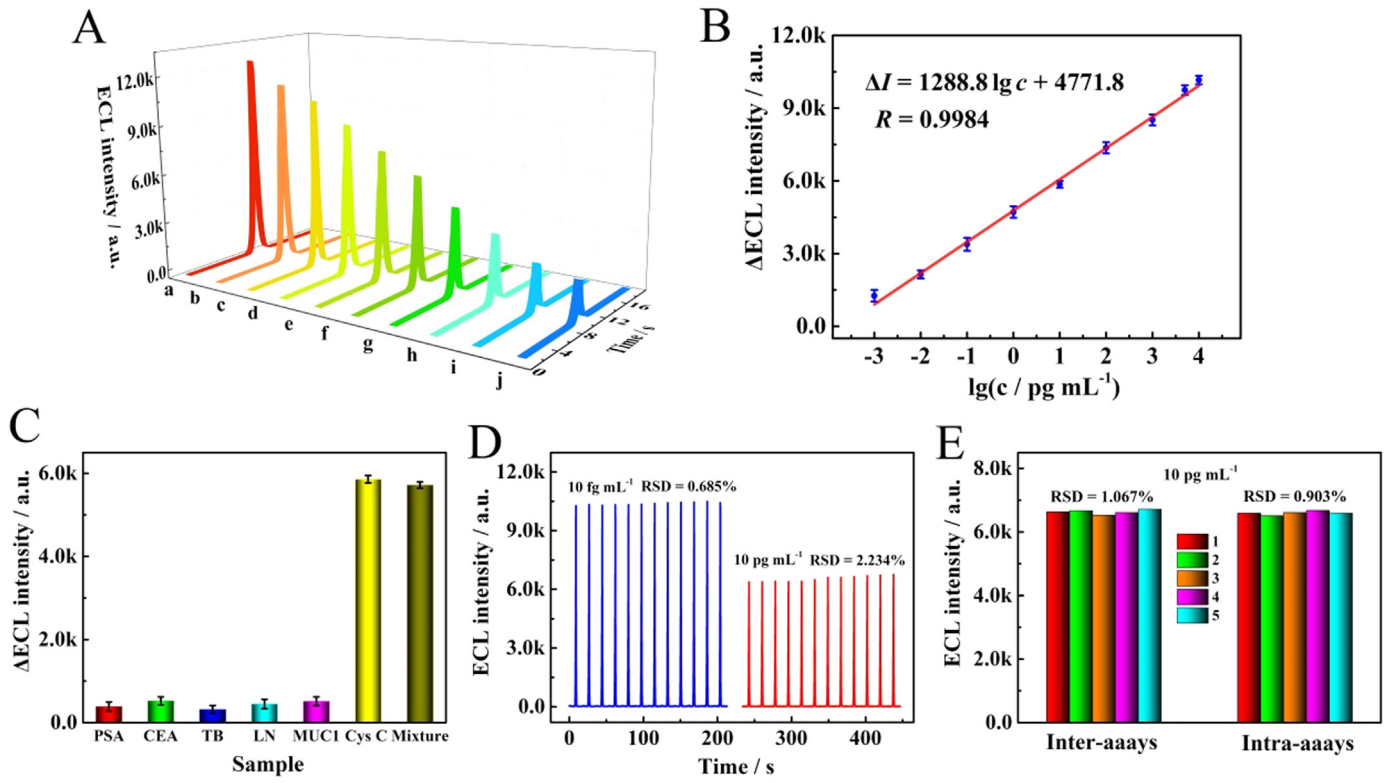

Fig. 5. (A) ECL intensity-time curves of the biosensor with different concentrations of Cys C. Cys C concentrations: (a) blank, (b) 1×10^{-3}, (c) 1×10^{-2}, (d) 1×10^{-1}, (e) 1, (f) 1×10^{1}, (g) 1×10^{2}, (h) 1×10^{3}, (i) 5×10^{3}, (j) 1×10^{4} pg mL^{-1}. (B) Relationship between the change of ECL intensity and the logarithm of Cys C concentration. (C) Comparison of △ECL responses with different targets: PSA (0.5 ng mL^{-1}), CEA (0.5 ng mL^{-1}), TB (0.5 ng mL^{-1}), LN (0.5 ng mL^{-1}), MUC1 (0.5 ng mL^{-1}), and Cys C (10 pg mL^{-1}), a mixture containing PSA (0.5 ng mL^{-1}), CEA (0.5 ng mL^{-1}), TB (0.5 ng mL^{-1}), LN (0.5 ng mL^{-1}), MUC1 (0.5 ng mL^{-1}), and Cys C (10 pg mL^{-1}). (D) ECL stability of proposed biosensor under consecutive cyclic potential scans. (E) Reproducibility of the proposed biosensor.

As shown in Fig. 5D, the biosensors had an excellent stability with relative standard deviations (RSD) of 0.685% and 2.234% of ECL peaks in 12 cycles.

To further investigate the reproducibility of the biosensor, inter- and intra-assays were performed. From Fig. 5E, the RSD (ECL response) of inter- and intra-assays are 1.067% and 0.903%, respectively, which demonstrated the excellent reproducibility of the developed biosensor.

3.9. Preliminary application of the ECL biosensor in real samples

To survey the preliminary application of the developed ECL immunoassay in human serum samples (obtained from the First Affiliated Hospital of Chongqing Medical University, China), lab study results of human serum samples were compared with those got by the turbidimetric immunoassay in clinical diagnosis. As displayed in Fig. S6, the correlation coefficient (R = 0.9947) and slope (0.9230) were close to 1, indicating that the lab study results by as-proposed ECL immunoassay were in good agreement with those by the clinical results. These results demonstrated that the developed ECL immunoassay had the potential application in the determination of Cys C in real samples.

4. Conclusions

In summary, an ultrasensitive “on-off” ECL immunoassay has been successfully developed for the serum Cys C detection based on the novel monolayer rubrene functionalized graphene composite (G/mRub) and immunorecognition-induced 3D DNA machine. The G/mRub not only possesses excellent ECL performance by maximizing the surficial Rub molecules but also provides prominent nanocarries with larger surface area and good electrical conductivity. Most importantly, the proposed ECL immunoassay shows a low limit of detection down to subfemtogram per milliliter level, which provides a universal approach for enzyme-free and ultrasensitive detection of proteins in human serum samples.

Acknowledgements

This research was supported by the National Natural Science Foundation of China (81873980 and 21804015), the Natural Science Foundation Project of CQ CSTC (cstc2018jcyjAX0206), Youth Project of Chongqing Municipal Education Commission Science and Technology (KJQN201800440), the China Postdoctoral Science Foundation (2017M622979) and Chongqing Special Postdoctoral Science Foundation (XmT2018073).

Declaration of interests

None.

Appendix A. Supplementary material

Supplementary data associated with this article can be found in the online version at https://doi.org/10.1016/j.bios.2018.12.009.

References

Alaboson, J.M.P., Wang, Q.H., Emery, J.D., Lipson, A.L., Bedzyk, M.J., Elam, J.W., Pellin, M.J., Hersam, M.C., 2011. ACS Nano 5, 5223–5232.
Cao, J.T., Yang, J.J., Zhao, L.Z., Wang, Y.L., Wang, H., Liu, Y.M., Ma, S.H., 2018. Biosens. Bioelectron. 99, 92–98.
Deng, S.Y., Hou, Z.T., Lei, J.P., Lin, D.J., Hu, Z., Yan, F., Ju, H.X., 2011. Chem. Commun. 47, 12107–12109.
Dick, J.E., Renault, C., Kim, B.K., Bard, A.J., 2014. J. Am. Chem. Soc. 136, 13546–13549.
Fumagalli, E., Raimondo, L., Silvestri, L., Moret, M., Sassella, A., Campione, M., 2011.

Chem. Mater. 23, 3246–3253.
Gan, S.Y., Zhong, L.J., Han, D.X., Niu, L., Chi, Q.J., 2015. Small 11, 5814–5825.
Gu, Z.J., Zhu, S., Yan, L., Zhao, F., Zhao, Y.L., 2018. Adv. Mater. e1800662.
Hercules, D.M., 1964. Science 145, 808–809.
Jayakumar, K., Camarada, M.B., Rajesh, R., Venkatesan, R., Ju, H.X., Dharuman, V., Wen, Y.P., 2018. Biosens. Bioelectron. 120, 55–63.
Jiang, X.Y., Wang, H.J., Wang, H.J., Zhuo, Y., Yuan, R., Chai, Y., 2017. Anal. Chem. 89, 4280–4286.
Khodakov, D.A., Khodakova, A.S., Linacre, A., Ellis, A.V., 2013. J. Am. Chem. Soc. 135, 5612–5619.
Lagos, A., Reyes, J., 1988. J. Polym. Sci. Pol. Chem. 26, 985–991.
Li, H., Li, M., Kang, Z., 2018a. Nanotechnology 29, 245604.
Li, N.X., Zheng, J., Li, C.R., Wang, X.X., Ji, X.H., He, Z.K., 2017a. Chem. Commun. 53, 8486–8488.
Li, Y.Y., Wang, A.G., Mason, S.D., Yang, X.L., Yu, Z.C., Tang, Y.N., Li, F., 2018b. Chem. Sci. 9, 6434–6439.
Li, W., Wang, L., Jiang, W., 2017b. Chem. Commun. 53, 5527–5530.
Liu, J.L., Tang, Z.L., Zhuo, Y., Chai, Y.Q., Yuan, R., 2017. Anal. Chem. 89, 9108–9115.
Liu, J.W., Lu, Y., 2006. Nat. Protoc. 1, 246–252.
Long, G.L., Winefordner, J.D., 1983. Anal. Chem. 55, 712A–724A.
Ma, P.Q., Liang, C.P., Zhang, H.H., Yin, B.C., Ye, B.C., 2018. Chem. Sci. 9, 3299–3304.
Pivetta, M., Blum, M.C., Patthey, F., Schneider, W.D., 2008. Angew. Chem. Int. Ed. 47, 1076–1079.
Qu, X.M., Zhu, D., Yao, G.B., Su, S., Chao, J., Liu, H.J., Zuo, X.L., Wang, L.H., Shi, J.Y., Wang, L.H., Huang, W., Fan, C.H., 2017. Angew. Chem. Int. Ed. 56, 1855–1858.
Repp, S., Harputlu, E., Gurgen, S., Castellano, M., Kremer, N., Pompe, N., Wörner, J., Hoffmann, A., Thomann, R., Emen, F.M., Weber, S., Ocakoglu, K., Erdem, E., 2018. Nanoscale 10, 1877–1884.
Seeman, N.C., 2010. Annu. Rev. Biochem. 79, 65–87.
Vinyard, D.J., Su, S.J., Richter, M.M., 2008. J. Phys. Chem. A 112, 8529–8533.
Wang, F., Willner, B., Willner, I., 2014. Top. Curr. Chem. 354, 279–338.
Watts, R.J., Dilly, S.E., 1996. J. Hazard. Mater. 51, 209–224.
Wu, J., Xianyu, Y., Wang, X., Hu, D., Zhao, Z., Lu, N., Xie, M., Lei, H., Chen, Y., 2018. Anal. Chem. 90, 4725–4732.
Yang, H., Chen, G., Cotta, A.A.C., N'Diaye, A.T., Nikolaev, S.A., Soares, E.A., Macedo, W.A.A., Liu, K., Schmid, A.K., Fert, A., Chshiev, M., 2018a. Nat. Mater. 17, 605–609.
Yang, J.M., Wu, Y.L., Gan, C.F., Yuan, R., Xiang, Y., 2018b. Biosens. Bioelectron. 117, 743–747.
Zeng, X.H., Wang, L.D., Duan, L., Qiu, Y., 2008. Cryst. Growth Des. 8, 1617–1622.
Zhang, P., Jiang, J., Yuan, R., Zhuo, Y., Chai, Y.Q., 2018. J. Am. Chem. Soc. 90, 6357–6361.
Zhao, M., Zhuo, Y., Chai, Y.Q., Yuan, R., 2015. Biomaterials 52, 476–483.
Zheng, J., Li, N.X., Li, C.R., Wang, X.X., Liu, Y.C., Mao, G.B., Ji, X.H., He, Z.K., 2018. Biosens. Bioelectron. 107, 40–46.
Zhu, L.Y., Liu, Q.H., Yang, B.Y., Ju, H.X., Lei, J.P., 2018a. Anal. Chem. 90, 6357–6361.
Zhu, W.J., Saddam Khan, M., Cao, W., Sun, X., Ma, H.M., Zhang, Y., Wei, Q., 2018b. Biosens. Bioelectron. 99, 346–352.